Evaluating the Importance of Nitrate-Containing Aerosols for the Asian Tropopause Aerosol Layer

Yunqian Zhu[1,2], Pengfei Yu[3], Xinyue Wang[4], Charles Bardeen[5], Stephan Borrmann[6,7], Michael Höpfner[8], Christoph Mahnke[6,9], Ralf Weigel[7], Martina Krämer[7,10], Terry Deshler[11,12], Jianchun Bian[10,13], Zhixuan Bai[13], Hazel Vernier[14,15], Robert W. Portmann[2], Karen H. Rosenlof[2], Corinna Kloss[14,16], Laura L. Pan[5], Warren Smith[5], Shawn Honomichl[5], Jun Zhang[5], Kane A. Stone[17], and Owen Brian Toon[4,18]

[1]Cooperative Institute for Research in Environmental Sciences, University of Colorado Boulder, Boulder, CO, USA, [2]Chemical Sciences Laboratory, NOAA, Boulder, CO, USA, [3]Jinan University, Guangzhou, China, [4]The Department of Atmospheric and Oceanic Sciences, University of Colorado Boulder, Boulder, CO, USA, [5]Atmospheric Chemistry Observations & Modeling, NSF National Center for Atmospheric Research, Boulder, CO, USA, [6]Particle Chemistry Department, Max Planck Institute for Chemistry, Mainz, Germany, [7]Institute for Atmospheric Physics, Johannes Gutenberg University, Mainz, Germany, [8]Institute of Meteorology and Climate Research (IMK-ASF), Karlsruhe Institute of Technology, Karlsruhe, Germany, [9]Now at Institute of Energy and Climate Research—IEK8, Forschungszentrum Jülich, Jülich, Germany, [10]College of Earth and Planetary Sciences, University of Chinese Academy of Sciences, Beijing, China, [11]The Department of Atmospheric Science, University of Wyoming, Laramie, WY, USA, [12]Now at Laboratory for Atmospheric and Space Physics, University of Colorado Boulder, Boulder, CO, USA, [13]Laboratory of Middle Atmosphere and Global Environment Observation, Institute of Atmospheric Physics, Chinese Academy of Sciences, Beijing, China, [14]Laboratoire de Physique et Chimie de l'Environnement et de l'Espace (LPC2E), CNRS/Université d'Orléans, UMR, [15]Université de Reims Champagne-Ardenne, GSMA, UMR CNRS, Reims, France, [16]Institute of Energy and Climate Research—IEK7, Forschungszentrum Jülich, Jülich, Germany, [17]Department of Earth, Atmospheric, and Planetary Sciences, Massachusetts Institute of Technology, Cambridge, MA, USA, [18]Laboratory for Atmospheric and Space Physics, University of Colorado Boulder, Boulder, CO, USA

Abstract The Asian Summer Monsoon (ASM) convection transports aerosols and their precursors from the boundary layer to the upper troposphere and lower stratosphere (UTLS). This process forms an annually recurring aerosol layer near the tropopause. Recent observations have revealed a distinct property of the aerosol layer over the ASM region, it is nitrate-rich. We present a newly implemented aerosol formation algorithm that enhances the representation of nitrate aerosol in the Community Aerosol and Radiation Model for Atmospheres (CARMA) coupled with the Community Earth System Model (CESM). The simulated aerosol chemical composition, as well as vertical distributions of aerosol size and mass, are evaluated using in situ and remote sensing observations. The simulated concentrations (ammonium, nitrate, and sulfate) and size distributions are generally within the error bars of data. We find nitrate, organics, and sulfate contribute significantly to the UTLS aerosol concentration between 15°–45°N and 0°–160°E. The two key formation mechanisms of nitrate-containing aerosols in the ATAL are ammonium neutralization to form ammonium nitrate in regions where convection is active, and condensation of nitric acid in regions of cold temperature. Furthermore, including nitrate formation in the model doubles the surface area density in the tropical tropopause region between 15°–45°N and 0°–160°E, which alters the chlorine partitioning and subsequently impacts the rate of ozone depletion.

Plain Language Summary The Asian Summer Monsoon can efficiently transport pollutants into the upper troposphere and form a layer of aerosols called the Asian Tropopause Aerosol Layer (ATAL). This research investigates the two key formation mechanisms for nitrate aerosol in the ATAL: one is due to cold temperature, and one is due to ammonium neutralization. The simulations are validated against in situ measurements. It also found that O_3 chemistry inside ATAL is influenced by nitrate aerosol.

1. Introduction

The Asian Summer Monsoon (ASM) convection transports pollutants from the boundary layer to the upper troposphere and lower stratosphere (UTLS) (Park et al., 2009; Randel et al., 2010). The aerosols and their precursors transported by the ASM form the Asian Tropopause Aerosol Layer (ATAL; Vernier et al., 2011), lasting from June to September, extending vertically from about 13 to 18 km, and horizontally between 0°–160°E and

15°–45°N. The ATAL has been observed by the Stratospheric Aerosol and Gas Experiment (SAGE) II satellite since 1999 (Thomason & Vernier, 2013). The Cloud-Aerosol Lidar and Infrared Pathfinder Satellite Observations (CALIPSO) provides evidence of enhanced backscatter of the ATAL after 2006 (Vernier et al., 2018). The presence of the ATAL affects the Earth's radiative balance, impacts cirrus cloud properties, and influences stratospheric ozone chemistry (Solomon et al., 2016; Vernier et al., 2018). Not until recently did in situ campaigns start to reveal the ATAL composition and aerosol microphysical properties in more detail (Appel et al., 2022; Bian et al., 2012; Höpfner et al., 2019; Mahnke et al., 2021; Pan et al., 2022; Schill et al., 2023; Vernier et al., 2018). In particular, the process of new particle formation plays a pronounced role in the region around the ASM and predominantly in altitudes of 12–16 km (Weigel, Mahnke, Baumgartner, Dragoneas, et al., 2021), even in the presence of ice cloud particles (Weigel, Mahnke, Baumgartner, Krämer, et al., 2021). The chemical composition, structural constitution, and morphology of individual refractory (i.e., non-volatile under atmospheric conditions) particles from the ATAL region were recently investigated (Ebert et al., 2023; Vernier et al., 2022).

Nitric acid-containing aerosols are known to form in the stratosphere due to cold temperatures in the winter polar vortex and likely near the tropical tropopause (Deshler, 2008; Hervig & McHugh, 2002) in the form of supercooled ternary solution (STS) and nitrate acid trihydrate (NAT). Satellite observations and aircraft measurements from the StratoClim campaign (https://www.stratoclim.org/, Appel et al., 2022; Höpfner et al., 2019; Krämer et al., 2020) reveal the presence of a different form of nitrate aerosol in the ASM UTLS: ammonium nitrate aerosol (AN). The Asian Summer Monsoon Chemical & CLimate Impact Project (ACCLIP) campaign (Pan et al., 2024) in situ observations further identified the distinct "nitrate-rich" behavior of the ATAL aerosols, which is different from the UTLS aerosol over North America (Schill et al., 2023). AN can exist at higher temperatures than STS and NAT (Lin & Tabazadeh, 2001, 2002) because AN effloresces rather than evaporates. In other words, when the temperature increases (i.e., relative humidity decreases), AN experiences a phase transition from liquid droplets to solid crystalline phase. Aside from the contribution of ammonium, the temperature in the ATAL also favors secondary aerosol condensation. Specifically, convectively driven tropopause cooling (Kim et al., 2018; Randel et al., 2015; Randel & Park, 2006) with frequent occurrence of cirrus clouds (Wang et al., 1996) is observed within the upper-level ASM anticyclone. Cold anomalies between 15 and 20 km are mainly due to hydrostatic adjustment to convective heating (Holloway & Neelin, 2007) and large-scale Kelvin wave response (Randel et al., 2003).

The data and ideas from these previous studies provide opportunities to evaluate model representations and understand the ATAL formation mechanisms. The two key formation mechanisms of nitrate-containing aerosols are the condensation of nitric acid due to the cold temperature, and the ammonium neutralization to form ammonium nitrate as secondary aerosol (i.e., not transported from the surface as primary aerosol), following convective transport of ammonia. The new algorithm has a focus on improving the representation of the ammonium neutralization mechanism, which was not represented well in our model previously. In this work, we present model simulations of ATAL using the CESM/CARMA aerosol model (Yu et al., 2015, 2022) with a newly developed nitrate aerosol formation algorithm in the UTLS. We aim to address three questions:

1. How well are the two formation mechanisms of nitrate aerosols in the ATAL represented in the model?
2. How well does our model reproduce the observed aerosol microphysical properties and compositions in the UTLS during the ASM season?
3. Does the enhanced nitrate aerosol impact stratospheric ozone chemistry?

Observations used in this study are discussed in Section 2. Section 3 describes the updated development of the nitrate aerosol formation algorithm. We evaluate our simulations against several groups of observations (Section 4.1) of aerosol composition, size distribution, and particle volume. Section 4.2 details how the extra surface area induced by nitrate aerosol can impact chlorine activation in the UTLS.

2 . Data From Space-Borne, Airborne and Balloon-Borne Observations

ATAL observations from four data sets are used for model evaluation. They include satellite remote sensing data from the limb sounder Michelson Interferometer for Passive Atmospheric Sounding (MIPAS) on board the polar orbiting satellite Envisat, balloon-borne optical particle counters (OPCs) data from the Balloon measurement campaigns of the Asian Tropopause Aerosol Layer (BATAL), balloon-borne in situ particle counters data from

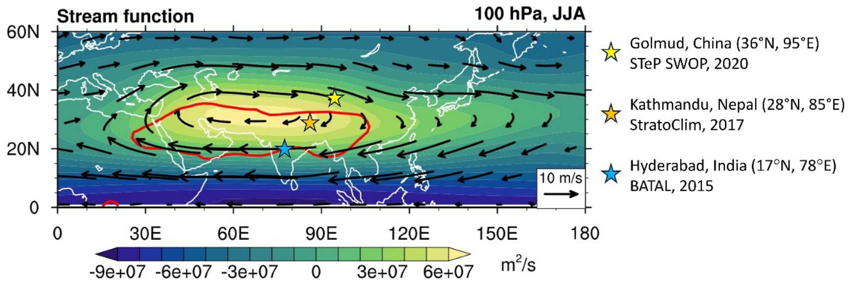

Figure 1. Wind vectors and the stream function (color contour) at 100 hPa averaged during June, July, and August (JJA), 2015 from model simulation. The locations of the three campaigns are marked with stars. The red contour line shows the interception of the tropopause with the 100 hPa pressure surface.

the Sounding Water vapor, Ozone, and Particle (SWOP) campaigns, and Airborne in situ measurement data from the Stratospheric and upper tropospheric processes for better Climate predictions (StratoClim) campaign.

MIPAS on board the polar orbiting satellite Envisat provided atmospheric emission spectra in the thermal infrared region between 685 and 2,410 cm^{-1} (Fischer et al., 2008). Here, we use the monthly ammonium nitrate (AN) and NH_3 concentration data retrieved from MIPAS (Höpfner et al., 2016, 2019). The MIPAS-detected NH_3 is retrieved from a 965 to 967 cm^{-1} band, and ammonium nitrate (AN) is retrieved from a band around 830 cm^{-1}. Uncertainties of the MIPAS AN mass concentration measurements are ±0.015 μg m^{-3} for single profile precision, ±30% ± 0.01 μg m^{-3} for systematic instrumental/retrieval, and ±30% due to uncertainties in AN spectroscopy. These values refer to the vertical resolution of MIPAS AN retrievals on the order of 3.5–4.5 km. Uncertainties of NH_3 are estimated to be ±5 pptv for single profile precision and ±15% for accuracy and also refer to a vertical resolution of 3.5–4.5 km in the upper troposphere (Höpfner et al., 2016).

Besides MIPAS, we compared the model results with data from three ASM in situ measurement campaigns. Figure 1 shows the locations of three campaigns and their locations relative to the ASM anticyclone. The ASM anticyclone is marked with the wind vector and its stream function. The 2015 BATAL balloon campaign explored particle concentrations and compositions with several balloon flights from 2014 to 2017 (Vernier et al., 2018, 2022). Here we use the aerosol size distribution data from optical particle counters (OPCs), 0.092–16.6 μm radius, from the University of Wyoming (Deshler, 2023). These particle measurements can include cirrus clouds with large particles. We exclude these cloud particles by subtracting particle numbers with sizes larger than 3 μm diameter. Concentration uncertainties are dominated by Poisson counting statistics with a minimum uncertainty of ±10%. Particle radius uncertainties of ±10% are dominated by pulse width broadening of the photomultiplier signals. Distribution moment uncertainties of ±40% for the lognormal size distribution fits are estimated from a Monte Carlo simulation accounting for uncertainties in particle size and number concentration (Deshler et al., 2003).

The StratoClim campaign was conducted in July and August 2017 over Nepal, India, Bangladesh, and the Bay of Bengal, covering altitudes up to 20 km. This work uses the data from the aerosol-related instruments including the ERC Instrument for the Chemical composition of Aerosols (ERICA) (Appel et al., 2022; Dragoneas et al., 2022; Hünig et al., 2022), a modified Ultra High Sensitivity Aerosol Spectrometer Airborne (UHSAS-A; particle diameter detection ranges from 65 nm to 1 μm) (Mahnke et al., 2021), the COndensation PArticle counting System (COPAS, for detecting total aerosol densities of sub-micrometer sized particles) (Weigel, Mahnke, Baumgartner, Dragoneas, et al., 2021; Weigel, Mahnke, Baumgartner, Krämer, et al., 2021; Weigel et al., 2009), and the New Ice eXpEriment—Cloud and Aerosol Spectrometer with Detection of POLarization (NIXE-CAS-DPOL, here referred to as NIXE-CAS, for particle diameter 0.61–50 μm) (Costa et al., 2017; Krämer et al., 2016). The data used here have been validated and detailed in Höpfner et al. (2019), Mahnke et al. (2021), and Appel et al. (2022).

As a key project of the Second Tibetan Plateau Scientific Expedition and Research, the STeP SWOP campaign (Bian et al., 2012; Li et al., 2017) was conducted by the Institute of Atmospheric Physics, Chinese Academy of Sciences in Golmud in the summer of 2020. Among the balloon-borne payload, a Portable Optical Particle Spectrometer (POPS) (Gao et al., 2016) was deployed to count particles between 70 nm and 1.5 μm in radius from the surface to the middle stratosphere (Yu et al., 2017).

3. CESM/CARMA With Enhanced Nitrate Aerosol Algorithm

3.1. Model Description

We use a sectional aerosol model, the Community Aerosol and Radiation Model for Atmospheres (CARMA), coupled with the Community Earth System Model (CESM) version 1 (Bardeen et al., 2008; Toon et al., 1988; Yu et al., 2015). The model includes most tropospheric and stratospheric aerosols and has been augmented with nitrate (Yu et al., 2022). In the model used by Yu et al. (2022), the nitrate aerosol condenses on sulfate and mixed particles kinetically, using the MOSAIC mechanism (Zaveri et al., 2008) between the surface and ∼300 hPa and Lin and Tabazadeh (2001) where the pressure levels are smaller than 300 hPa (i.e., upper troposphere and above). However, Lin and Tabazadeh (2001) do not consider the solid phase of ammonium particles (ammonium sulfate and ammonium nitrate), which has been added to this model version.

We define two groups of aerosols with 20 discrete size bins for each group: the sulfuric acid particle group with a radius ranging from 0.2 nm to 1.3 μm; and the mixed particle group with a radius from 1 nm to 10 μm to be more suitable to represent the growth process of nitrate aerosol. The sulfuric acid particle group contains sulfuric acid and includes homogeneous nucleation and condensational growth of sulfuric acid gas. The mixed particle group contains sulfate, organics, black carbon, dust, sea salt, ammonium, and nitrate. The secondary organic aerosol is treated using the bulk scheme (Yu et al., 2015). The mixed group includes the condensational growth of sulfuric acid, ammonia, and nitric acid. Intra-group and inter-group coagulation of particles is considered. Water vapor is assumed to stay in equilibrium with the gas phase for all groups of particles.

For nitrate condensational growth on mixed particles, we treat it identically to that for supercooled ternary solution growth in polar stratospheric cloud simulations (Zhu et al., 2015), in which HNO_3 and H_2SO_4 weight percent are calculated using the formulation of Luo et al. (1995). The weight percent of H_2SO_4 considered sulfuric acid mass in both sulfate and mixed group. The vapor pressure of HNO_3 is calculated using Luo et al. (1995), and H_2SO_4 using Ayers et al. (1980). In addition, we allow ammonium nitrate and ammonium sulfate efflorescence and deliquescence based on the aerosol thermodynamics model (AIM) (Carslaw et al., 1995; Clegg et al., 1992, 1998; Massucci et al., 1999; Wexler & Clegg, 2002). The AIM model calculates the gas/liquid/solid partitioning in aerosol systems including inorganics (such as H^+, NH_4^+, Na^+, K^+, Mg^{2+}, Ca^{2+}, SO_4^{2-}, NO_3^-, Cl^-, Br^-, OH^-, CO_3^{2-}, etc.), organic components and water.

Figure 2 shows an example of the formation of UTLS aerosol at 100 hPa with NH_3 (10 pptv and 1 ppbv), HNO_3 (2 ppbv), and H_2SO_4 (0.1 ppbv). This figure highlights the equilibrium temperature of coexistence for sulfate, nitrate, and ammonium species, and how much the HNO_3 and NH_3 gasses are partitioned into different condensed phases as a function of temperatures. The aerosol formed at different ambient temperatures between 185 and 220 K. The tropical and subtropical UTLS usually has temperature >190 K, while 185 K is more typical for stratospheric polar night. In the UTLS, it is possible to form liquid phase NH_4^+, NO_3^-, HSO_4^- and SO_4^{2-} solutions, as well as solid crystals such as NH_4NO_3, NH_4HSO_4, and $(NH_4)_3H(SO_4)_2$. Lin and Tabazadeh (2002) show that HNO_3 dissolution in ammoniated aerosol solutions can prevent the efflorescence of $(NH_4)_2SO_4$ and NH_4HSO_4 salts in favor of $(NH_4)_3H(SO_4)_2$ (known as letovicite) crystallization. In the tropical UTLS, ammonium is all in the condensed phase because of the cold temperature. Figures 2a and 2c indicate three temperature ranges for neutralized ammonium species: (a) When temperature is above 196 K, NH_4^+ prefers to form ammonia-sulfur compounds, and the excess NH_4^+ prefers to form AN; (2) When the temperature is below 196 K and above 195 K, ammonia-sulfur compounds deliquesce, and NH_4^+ prefers to form AN; (3) When the temperature is below 195 K, the solid phase NH_4NO_3 gradually deliquesces as the liquid phase NO_3^- gradually condenses as the temperature decreases.

Based on the thermodynamic model results, we implement simplified efflorescence and deliquescence parameterizations for AN and ammonium sulfate (AS) formation: for the UTLS from 70 to 150 hPa, all the NH_3 will be in the aerosol phase. It will combine with SO_4^{2-} first to form $(NH_4)_3H(SO_4)_2$, and the rest will combine with NO_3^- to form NH_4NO_3. When the temperature is below 196 K, $(NH_4)_3H(SO_4)_2$ deliquesces and SO_4^{2-} dissolves in the liquid aerosol. All NH_4^+ is available to form NH_4NO_3 or dissolve in the liquid solution NO_3^{2-} based on the formulation of Lin and Tabazadeh (2001).

For this study, we ran simulations for the years 2015, 2017, and 2021 to compare with the three measurement campaigns detailed below. The model runs with using annually repeating surface emissions of 2000 and an explosive volcanic emissions inventory from 2015 to 2021, to account for variability and trends in the volcanic

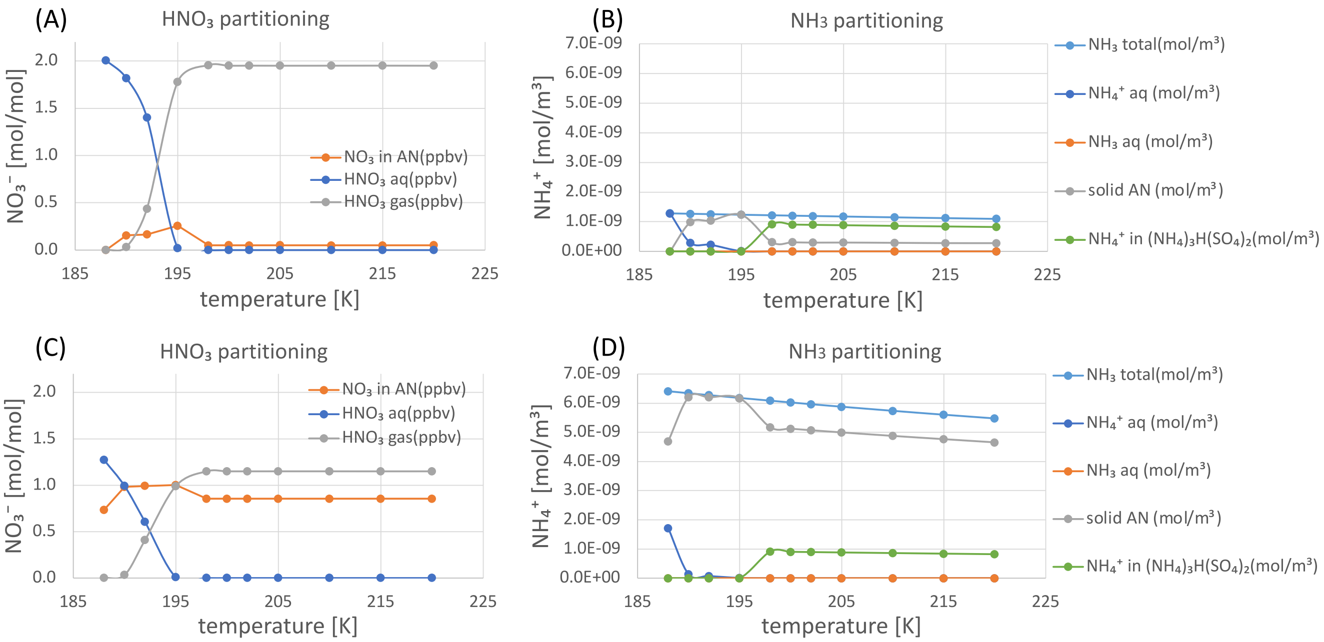

Figure 2. The partitioning of HNO_3 (a and c) and NH_3 (b and d) at UTLS temperatures using the E-AIM model (aim.env.uea.ac.uk) assuming NH_3 of 10 pptv (Panel a and b) and 1 ppbv (Panel c and d), HNO_3 of 2 ppbv and H_2SO_4 of 0.1 ppbv. The panels (a and c) show the HNO_3 partitioning in the form of gas phase HNO_3, AN and aqueous solutions. The panels (b and d) show the NH_3 partitioning in the form of aqueous phase NH_4^+, aqueous phase NH_3, AN, and $(NH_4)_3H(SO_4)_2$.

sulfate contribution to the background sulfate burden (Neely et al., 2013; Vernier et al., 2011). The explosive volcanic emission inventory follows Mills et al. (2016) and Neely et al. (2016) with updates until 2022. The model 5-year spin-up and simulations from 2015 to 2021 are nudged with Goddard Earth Observing System 5 (GEOS5) (Rienecker et al., 2008) assimilated data every 30 min. Compared to Yu et al. (2022), the current scheme allows more NH_3 to enter the UTLS following Wang et al. (2022), who found that 10% of boundary layer NH_3 is lofted to the upper troposphere by deep convective systems. This hypothesis assumes the volatile chemicals can dissolve in the cloud droplets and release in the outflow of the ice cloud in the upper troposphere (Jost et al., 2017), which is still highly uncertain. In our model, we simply tune the solubility factor to allow 10% of NH_3 to be transported to the upper troposphere without involving any cloud parameterization.

3.2 . Formation Mechanisms for ATAL Nitrate-Containing Aerosols in Observations and in the CARMA Model

In this section, we examine how well the two key formation mechanisms of nitrate-containing aerosols are represented in the newly developed nitrate scheme: the condensation of nitric acid due to the cold temperature, and the ammonium neutralization to form ammonium nitrate. We begin by demonstrating how the two types of nitrate aerosols have distributions associated with different background structures in the ASM UTLS. Specifically, the distribution of aerosol from nitric acid condensation is related to the temperature distribution. We identify the background condition for the formation region using a 195 K temperature threshold. The formation of the ammonium nitrate is associated with the ASM convective transport of lofted ammonia. We identify this region using the "bulging" ASM tropopause (Pan et al., 2016). Identification of these physical relationships is a critical step for this work. The physical conditions identified for the two types of aerosol formation enable the model-data comparison based on the characteristics of the controlling mechanisms. This concept is demonstrated in Figure 3.

Figure 3 shows the two types of nitrate aerosols formed in the ASM UTLS as secondary aerosols: total condensed NO_3^- in Figure 3a, AN in Figure 3b, and nitric acid in ternary solution in Figure 3c. Figure 3b clearly shows the high AN center and the shape of the high ammonium contour (yellow contour) is collocated with the tropospheric "bubble" (green contour), which is a bubble of tropospheric air above the global mean tropical tropopause created by the ASM. At 100 hPa, the tropopause contour marks the region of bulging tropopause driven by the ASM convection (Bian et al., 2012; Pan et al., 2016). Figure 3c shows high concentrations of NO_3^- collocated with

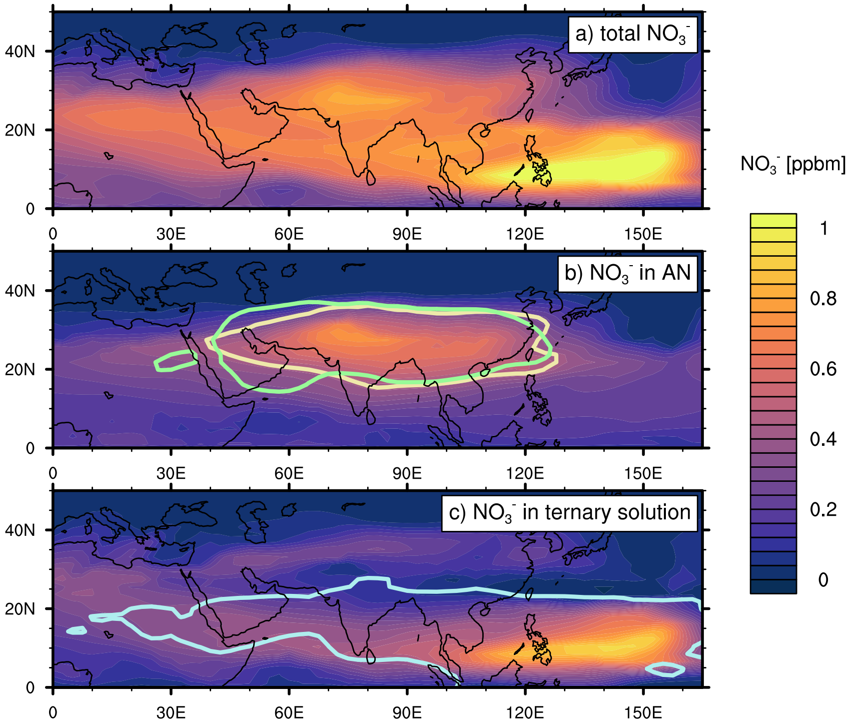

Figure 3. Simulated condensed NO_3^- concentration at 100 hPa averaged over the first 10 days of August 2017. (a) total condensed NO_3^-; (b) Solid AN. Within the yellow contour is the region where the average total NH_3 and NH_4^+ is above 120 pptm. The intersection of the tropopause crossing the 100 hPa contour is shown in green. (c) The condensed NO_3^- in the ternary solution ($HNO_3/H_2SO_4/H_2O$). The averaged 195 K temperature contour is shown in blue.

temperatures lower than 195 K (blue contour) near the west Pacific Ocean and south of 20°N, which is mainly outside of the ASM anticyclone. The condensation of NO_3^- near the cold tropical tropopause is similar to what occurs in polar stratospheric clouds. Tropical nitric acid clouds have been proposed in the past and been retrieved by the Halogen Occultation Experiment (Hervig & McHugh, 2002). One thing to note is that low concentrations of NO_3^- exist outside these tropopause, ammonium, and temperature contours. For AN, it is because low concentration of NH_3 exists outside the contour region. For non-ammonium nitrate particles, in addition to the time averaging in the figure which tends to artificially spread out condensed NO_3^-, there is a known issue with the model: Zhu et al. (2015) show that when the surface area density is lower than 4 $\mu m^2/cm^3$, the particles are unlikely to stay in equilibrium. In other words, when the condensed NO_3^- concentration is low, it takes time to grow and evaporate to its equilibrium states which we will investigate more in the future.

The spaceborne and balloon observations have shown evidence to support these two formation mechanisms (cold temperature and ammonium neutralization near convectively active regions) as both being important for the UTLS NO_3^- formation. Figure 4 shows the MIPAS observations of AN averaged at 16 km (near 100 hPa) in multiple years of MIPAS operations. Note that liquid-phase nitrate-containing particles are not part of the retrievals in MIPAS observations, so the composition retrieved by MIPAS is equivalent to Figure 3b. The year-to-year variations indicate the AN amount is highly dependent on the amount of NH_3 transported to the ASM. Similar to the simulated AN in Figure 3b, the location of MIPAS AN is well collocated with the tropopause contour, which marks regions of active convection. According to Vernier et al. (2022), balloon observations during the 2017 BATAL campaign showed a substantial amount of nitrate aerosols (94 ng/m^3 in standard atmosphere) at 16 and 17 km altitude. This suggests the presence of nitrate-containing particles that do not include NH_4^+ ions, such as ternary solutions or solids consisting of HNO_3 and H_2O in the ATAL.

Characteristically, the model simulates the ammonium nitrate and non-ammonium nitrate particles reasonably well corresponding to the chemical and atmospheric structures. In the following sections, we conduct quantitative comparisons of the model with the in situ observations.

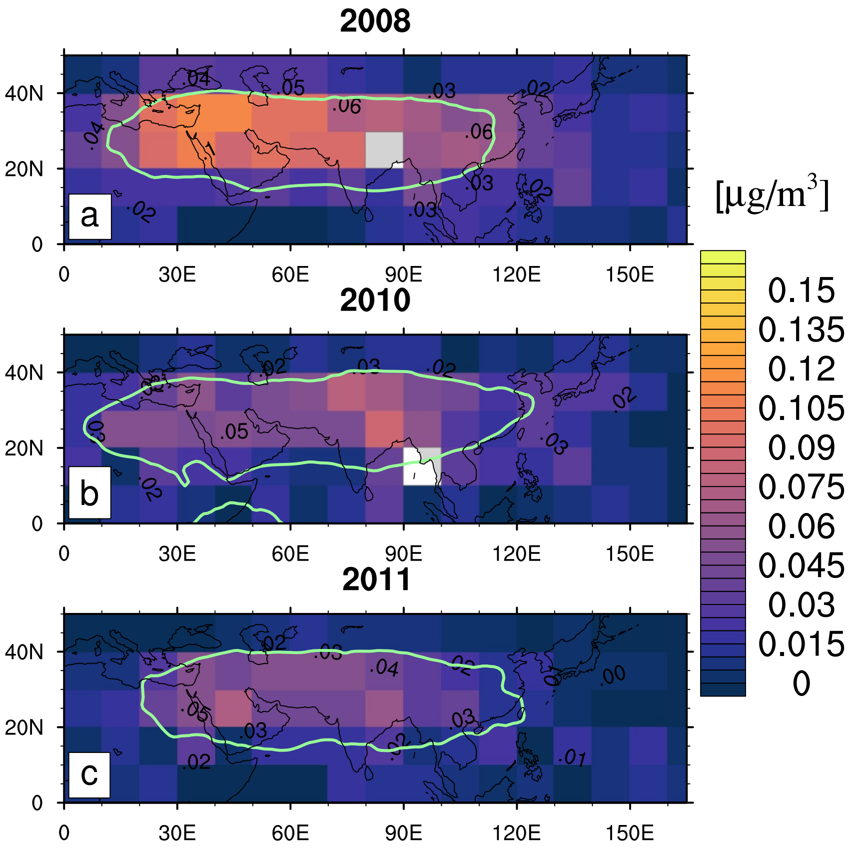

Figure 4. MIPAS observed AN (Höpfner et al., 2019) at 16 km in August during multiple years of its operation. The green contour indicates the region where the tropopause crosses 16.3 km, which marks the edge of the bulging tropopause driven by the ASM convection.

4. Quantitative Comparison With Data

4.1. Aerosol Composition

It is a big challenge for climate models to simulate the ATAL composition. Different models previously gave different estimates with various compositions (Bossolasco et al., 2021; Fadnavis et al., 2013; Gu et al., 2016; Yu et al., 2015), such as sulfate, nitrate, primary organics, black carbon, mineral dust, and secondary organics. Modeling aerosol composition in the ASM UTLS is difficult because it is related to many complicated processes: the surface emissions of pollutant precursors, the solubility of different chemicals, the convection scheme in the model, and whether the model contains a sufficient formation mechanism of secondary aerosols. In this section, we evaluate our modeled aerosol composition using the StratoClim in situ measurements, MIPAS AN, and NH_3 measurements. Then we discuss the general aerosol compositions and their formation mechanisms throughout the ASM UTLS.

Figure 5 shows mass concentrations from the model simulation (dashed line) and ERICA observations (solid line) during the 2017 StratoClim campaign. Both the observational data and the simulation show a clear ATAL between 360 and 420 K with peaks in several constituents between 360 and 390 K. The simulated concentrations of ammonium, nitrate, and sulfate are generally within the error bar of the observations. The difference for the height of the peak values may be due to the low vertical resolution of the model, which is about 1 km in the UTLS. Also, there is a considerable flight day to flight day variability in the vertical profiles (Appel et al., 2022). It is also likely due to the difficulty to accurately represent altitude of convective outflow in the climate model, which is because the convection is not explicitly resolved with typical coarse climate model grid spacing. The model simulates nitrate in the form of a ternary solution (blue dotted line) and AN (blue dot-dash line). Figure 5 shows that AN is dominant. The model overestimate of the organics in the stratosphere by about a factor of 2 may be because the secondary organics in this version of the CESM/CARMA model are treated using a simplified secondary organic

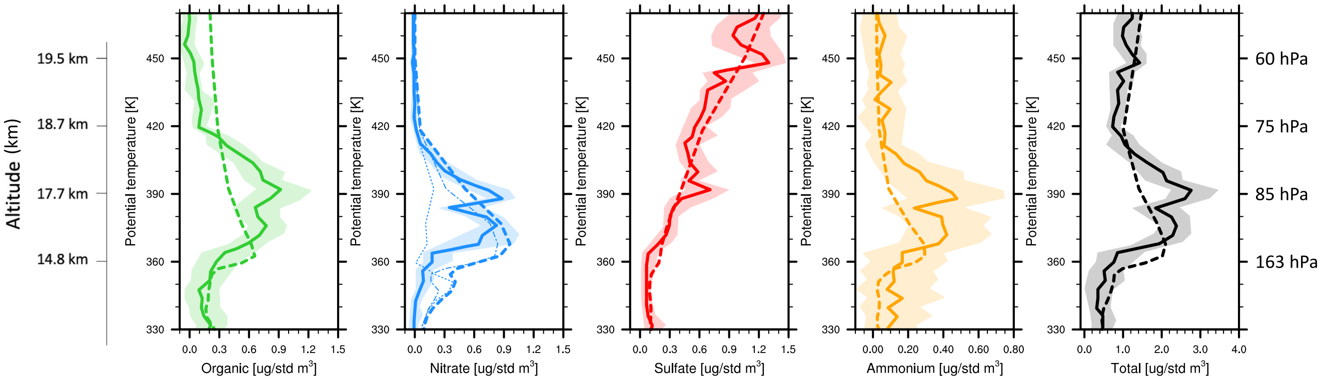

Figure 5. Aerosol composition from the simulation (dashed lines) compared with ERICA (solid lines) from the entire StratoClim aircraft campaign in 2017 (Appel et al., 2022). The ERICA data are averaged from the entire StratoClim aircraft campaign in 2017 every other day from July 27 to August 10 (eight flights). The simulated values are averaged over the region between 21°–28°N and 81°–88°E (approximately the flight region), and every other day from July 27 to August 10. The blue dotted line is nitrate in the form of ternary solution and the blue dot-dash line is nitrate in the form of AN from the model. The shaded area is the ERICA 25th/75th percentiles at given potential temperature.

aerosol parameterization (Yu et al., 2015). The sulfate aerosol mixing ratio increases upwards since its main source is stratosphere, therefore it doesn't have a clear peak in the ATAL.

Figure 6 shows the simulated averaged aerosol composition in the ATAL (averaged over 0°–160°E and 15°–45°N). Organics, nitrates, and sulfates are the dominant types of aerosols, with nitrate peaking near 16 km, organics peaking near 15 km, and sulfate peaking in the stratosphere. At 16 km, most of the nitrate can be neutralized by the available ammonium (the molar mass ratio of NO_3/NH_4 is 3.44). Other aerosols (dust, sea salt, black carbon) in Figure 6 have minimal mass mixing ratios in the UTLS and stratosphere (gray, almost invisible in the graph). It indicates many primary aerosols can be washed away before reaching the UTLS, but with exemptions such as dust storms (Yang et al., 2022). This result is consistent with the conclusion from Yu et al. (2017) that deep convection systems effectively remove primary aerosol.

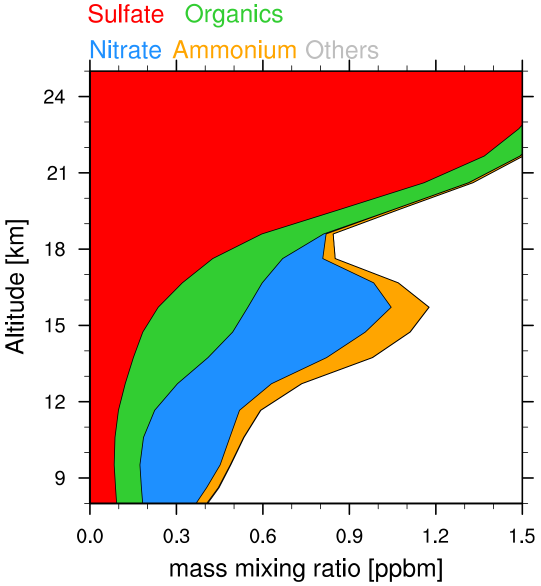

Figure 6. The simulated aerosol composition mixing ratio averaged over 0°–160°E, 15°–45°N, for sulfate (red), organics (green), nitrate (blue), ammonium (orange), and others (gray, sum of black carbon, sea salt and dust). The area of each color represents the mixing ratio of the corresponding species.

4.2 . Aerosol Microphysical Properties

Particle size distributions can help to calculate aerosol volumes, surface areas, numbers, and optical properties, which are important for aerosol budget, heterogeneous chemistry, and radiative forcing estimation. Figure 7 compares the simulated particle size distribution with balloon observations (the Wyoming OPC) over Hyderabad, India, during the 2015 BATAL campaign. The shapes of the curves for particles smaller than ~1 μm are mostly within the error bars of the observations at 15 and 17 km where the ATAL typically peaks. At 19 km, the simulated number size distribution is slightly lower than observation for particle radius larger than 0.5 μm. As mentioned in Section 3, we have filtered out particles above 3 μm diameter from the observations (open circles) to eliminate cirrus clouds suggested by the NIXE-CAPS measurement in this area (Krämer et al., 2016, 2020).

Figure 8 shows that the simulated particle size distributions (red bars) are generally within the error bars of the measurements during the 2017 StratoClim campaign. The red bars are particles dominant with mixed sulfate, nitrate, ammonium and organics. The blue bars are the particles dominant with sulfate binary. We can see that sulfate binary dominant aerosol is mainly below 0.1 μm. We find that to create the close match with the measurements requires that nitrate aerosol growth be taken into account. Additional comparisons with nitrate and particle volume during the StratoClim campaign are shown in Figure A1. Comparing the 17 km (ATAL region) and 20 km (stratosphere) in Figure 8, we can see the particle number concentration in the

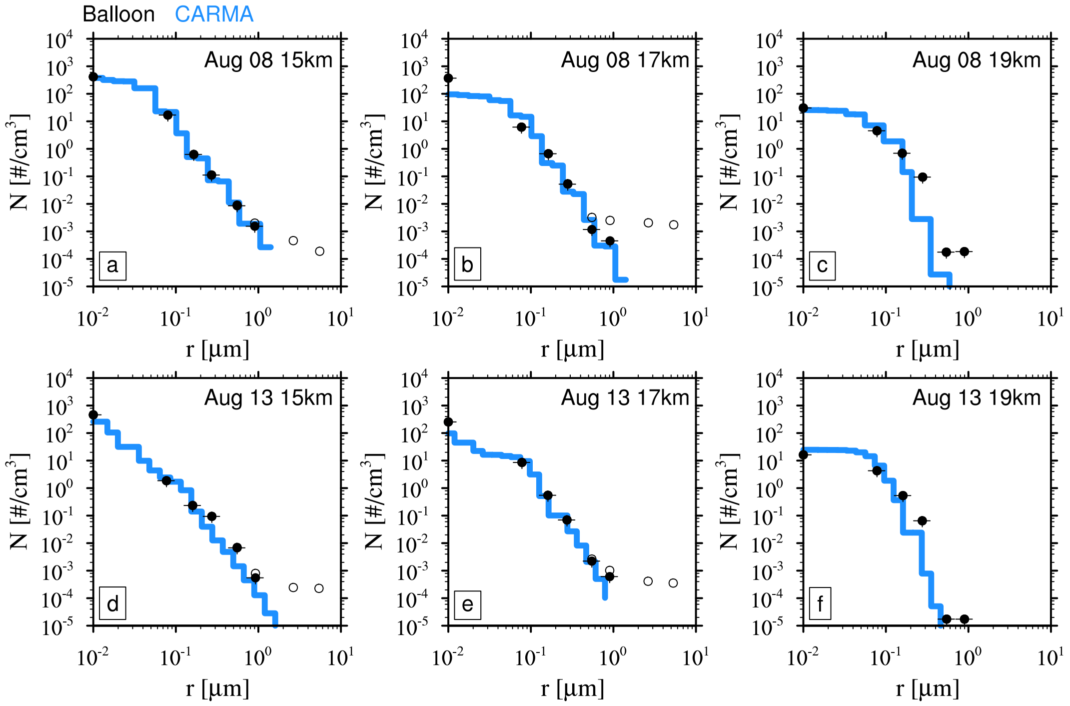

Figure 7. The number concentrations that are larger than a particular radius from the BATAL balloon observation over Hyderabad, India (17°N, 78°E) (black dots), and from the model at the nearest location (18°N, 77.5°E) (blue line). Black rimmed circles are the original observations including both aerosol and cloud particles. The black dots eliminate particles with diameter >3 µm.

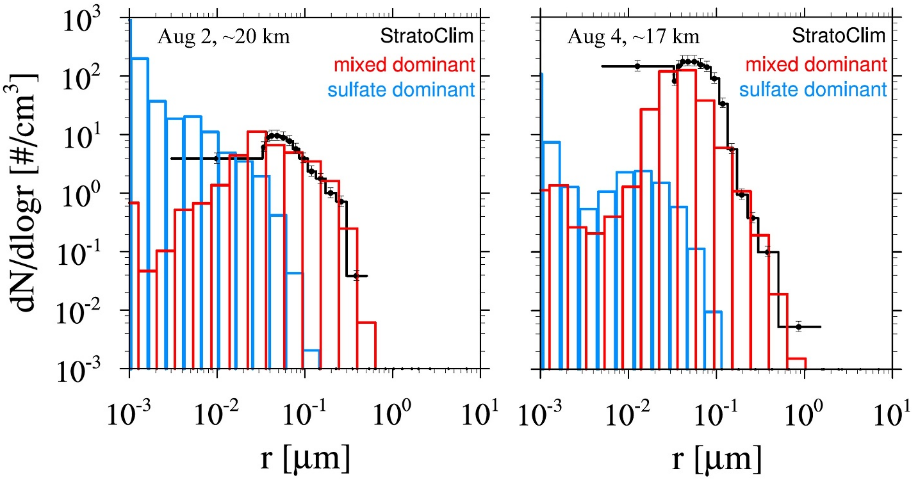

Figure 8. The simulated size distribution compared with combined measurements from the COPAS, UHSAS-A, and NIXE-CAS instruments during two flights (left panel: 2 August 2017, ~56 hPa; right panel: 4 August 2017, ~90 hPa) of the StratoClim Campaign (Mahnke et al., 2021). The blue bars are the particles with compositions dominated by sulfate binary; the red bars are the particles with compositions dominated by mixed sulfate, nitrate, ammonium and organics. The modeled results are picked from the same days and nearby location as observed: left panel on August 2, altitude between 20.6 and 19.6 km (pressure level 52–61 hPa) averaged over the area between latitude 27.5°–29°N and longitude of 80°–85°E; right panel on August 4, altitude between 16.8 and 17.8 km (pressure level 85–100 hPa) averaged over the area between latitude 27.5°–29°N and longitude of 80°–85°E. Note that the total simulated aerosol number should add mixed particles and sulfate together. However, the need to add them together is trivial because we use the lognormal scale.

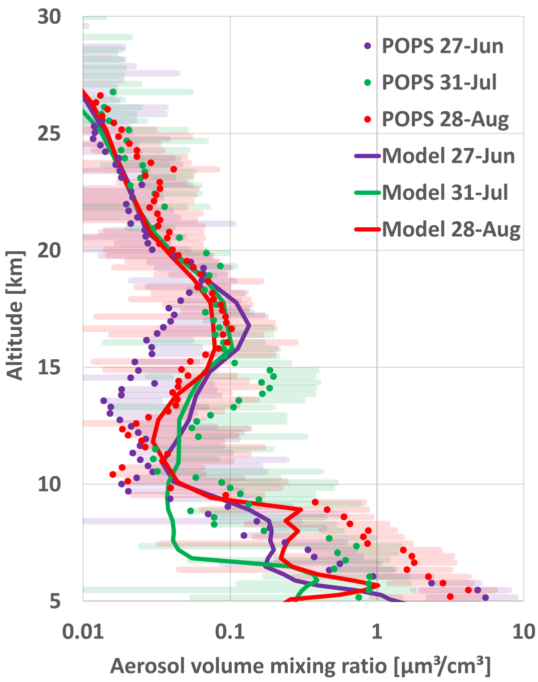

Figure 9. Dotted lines show POPS measurement at Golmud during the 2020 STeP SWOP campaign at 36.4°N and 94.9°E for three particular days: June 27, July 30, and August 27. Solid lines are from the simulation at the closest model grid box (37°N, 95°E) and days. The error bars represent the standard deviation when we average values over vertical spacing for POPS.

ATAL is one order of magnitude higher than the stratospheric aerosol concentration.

Figure 9 shows the particle total mass mixing ratio compared with POPS measurements during the 2020 STeP SWOP campaign. The simulated mass mixing ratio maximum is within a factor of two of the observed mixing ratio in the ATAL. However, the altitude of the peak mixing ratio in the measurement varies over altitude during these 3 days while the modeled ATAL mixing ratio consistently peaks at 16–18 km. This measurement is very valuable because the location is in the northern branch of the ASM anticyclone. The high temperature there prohibits the condensation of HNO_3 to form non-ammonium nitrate particles; rather, AN formation is critical to reproduce the ATAL signals. The noticeable difference of the ATAL peak high is again shown in this measurement. As we explained above for the ERICA comparison in Figure 5, The difference may be due to the low vertical resolution of the model, as well as the difficulty to accurately resolve convection with coarse climate model grid spacing.

4.3. Chemical Impacts of the ASM Revealed by Simulated Nitrate Aerosol Enhancement

Solomon et al. (2016) suggested that heterogeneous chlorine chemistry in the ASM region cannot be neglected. The anticyclonic circulation of the ASM in the UTLS mixes ATAL air masses that have large particle surface areas to the subtropics where they are added to the aerosol condensed at the top of the cold Tropical Transition Layer, TTL. The cold temperatures and large particle surface areas provide preferred conditions for heterogeneous chlorine chemistry that leads to ozone depletion. Here, we compare simulations of chlorine species partitioning with and without nitrate formation. The extra nitrate formed in the ASM and TTL makes the particles more like liquid polar stratospheric clouds (i.e., supercooled ternary solution, STS) and provides an additional surface area to activate the chlorine in the TTL near the southern branch of the anticyclone. As shown in Figures 10–10a3, the surface area approximately doubled due to extra nitrate formed in the model from 0° to 40°N and from 0° to 180°E at 100 hPa. Figure 10 also shows ClO increases by ∼15 pptv in the southern branch of the ASM anticyclone near 15°N; and HCl decreases by ∼20 pptv relative to the simulation without nitrate. $ClONO_2$ shows a belt of decrease near 10°N by ∼5 pptv and increase at other places, especially over mediterranean (∼10 pptv increase). The $ClONO_2$ anomaly depends on the partitioning of Cl and HCl into $ClONO_2$ and ClO driven by reaction speed of the heterogeneous chemistry. The simulation calculated the reactive uptake probability (γ value) of HCl + $ClONO_2$, which over the Philippines is quite large (∼0.1) but over the Mediterranean is quite small (∼0.0006). O_3 changes relative to the simulation without nitrate are very subtle (less than 5% decline) between 0° and 30°N. The area north of 30°N where the temperature is higher and nitrate surface area is low experiences no decline in ozone. The largest O_3 decrease is located on the edge of the southern ASM region flowing into the Western Pacific, which is consistent with the area where the strongest heterogeneous reaction occurs (largest HCl and $ClONO_2$ decreasing in Figures 10b3 and 10d3). The southward flow around the Asian monsoon brings high levels of inorganic chlorine into this region (Solomon et al., 2016) where there's a high surface area density increase (Figure 10a3) and the lowest temperature (Figure 10f1). Note that in this model version, we simply assume the particles have the same acidity as sulfuric acid particles or STS to determine the reaction rate of heterogeneous chemistry. We haven't considered the acidity change due to NH_4^+ in the solution or particle phase change when solid AN and AS formed. Changing the acidity of the aerosol will likely change the acid-catalyzed second order rate constants for the heterogeneous reactions (lower acidity equals a slower second order reaction rate) and change the solubility of HCl through altering the ability for HCl to dissociate (HCl will dissociate more in a less acidic solution), which deserves further exploration in the laboratory. Adding ammonium in the particle likely increases the basicity of liquid phase particles which will increase the heterogeneous reaction rates through increased HCl solubility. This effect will be largest at temperatures >192 K, as the reaction probabilities will be approaching 1 below this value (Shi et al., 2001).

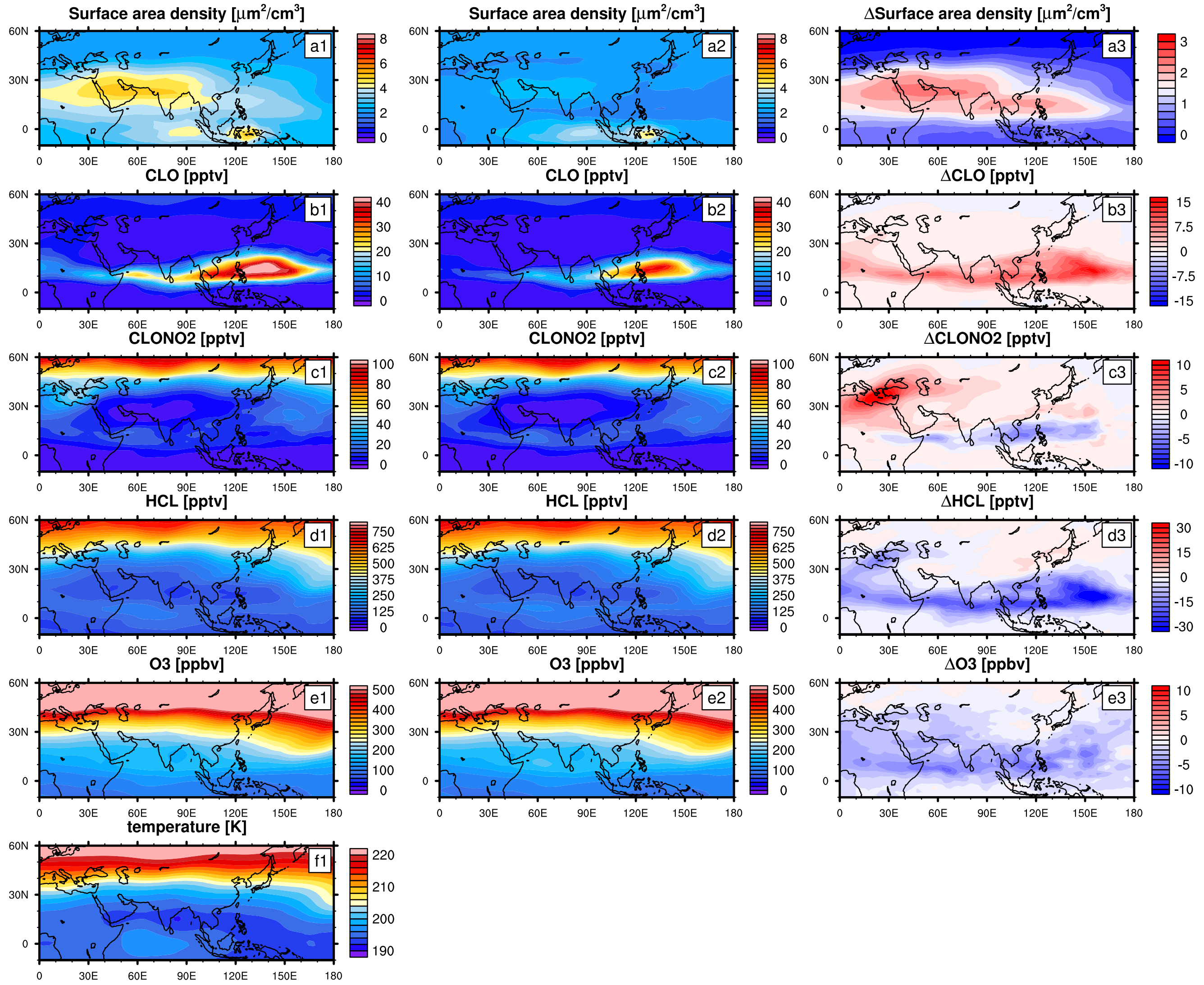

Figure 10. Simulated chemicals with nitrate (left column) and without nitrate (middle column) and percentage increase/decrease due to adding nitrate to the model (right column) at 100 hPa. Row a: surface area density; Row b: ClO; Row c: $ClONO_2$; Row d: HCl; Row e: O_3; Row f: Temperature.

5. Conclusion

This work highlights a new development in the CESM/CARMA model for representing nitrate-containing aerosol formation processes. The simulations are consistent with ASM observations regarding particle microphysical properties. The improved model produces simulated concentrations (ammonium, nitrate, and sulfate) and aerosol size distributions are generally within error bars. The simulations and observations show that nitrate, and sulfate are major contributors to UTLS aerosols in the ASM region. Primary aerosols such as black carbon, dust, and sea salt, are minor, less than 1% of the total aerosol mass. The nitrate aerosols in the ATAL are in the form of AN in the region where active convection transports NH_3 gas to the upper troposphere while in another region the nitrate aerosols are in the form of ternary solution ($H_2SO_4/HNO_3/H_2O$) due to the local cold temperatures. The additional nitrate-containing aerosols provide surface area and impact the chlorine partitioning in the ASM UTLS, slightly decreasing ozone. We found that the model overestimates secondary organics in the stratosphere by a factor of about 2, likely due to the simplified secondary organic aerosol parameterization in the current model version. In the next generation of models, we will improve our secondary organic aerosol representations by using a sectional framework (Tilmes et al., 2023) for them instead of a bulk model as in the current version. With the bulk scheme, it is difficult to calculate the aerosol extinction and radiative property due to lack of particle number and size information. Also, previous studies suggest different formation pathways of nitrate containing aerosols inside convective ice clouds due to lightning induced NO_x (Bela et al., 2016), which can be explored in the future model development. In addition, we will develop algorithms to include the heterogeneous reaction rate considering the acidity and phase change due to the formation of ammonium aerosols. This investigation will be similar to the method stated in Solomon et al. (2023), which update the acidity of particle due to organics mixed in the sulfate aerosol. With the major UTLS aerosols implemented in the model, CESM/CARMA will be a useful tool to understand the evolution of UTLS aerosols and their radiative impact in historical and future climate.

Appendix A: The Additional Comparisons Between StratoClim Measurements and the Model Simulations

The figures shows the comparisons between StratoClim particle compositions and volumes and the simulated ones, which shows reasonable agreement that is consistent with the comparisons in the main content.

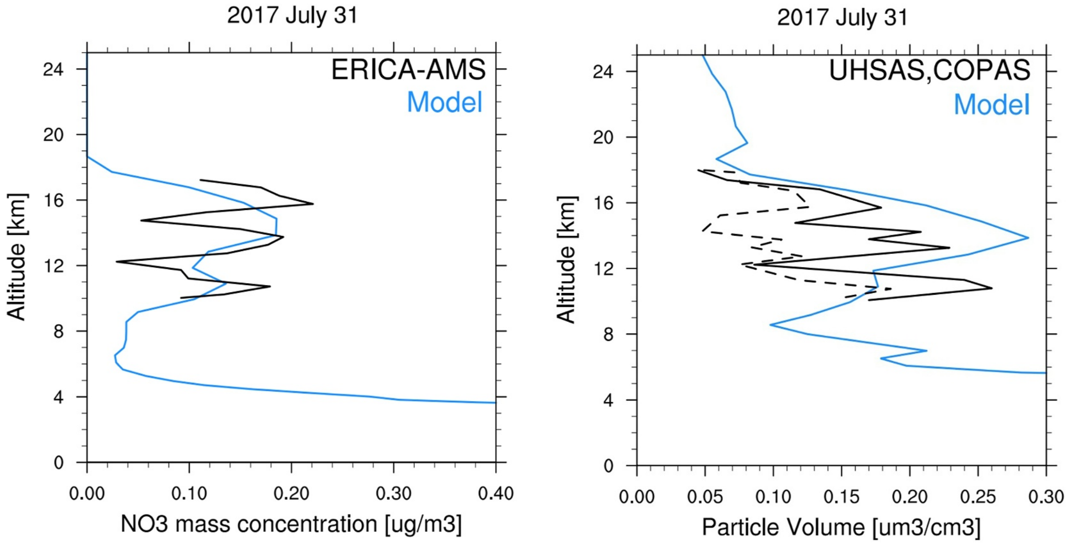

Figure A1. Particulate NO_3 mass concentration (left panel) and aerosol particle volume density (right panel; during the ascent (dashed black line) and the descent (black line) at Kathmandu) from the StratoClim campaign (Höpfner et al., 2019) compared with the model.

Data Availability Statement

The E-AIM model is available at http://www.aim.env.uea.ac.uk/aim/aim.php. MIPAS data is available at https://doi.org/10.5445/IR/1000095498. ERICA mass spectrometry data are available from the Edmond database (https://doi.org/10.17617/3.8x). The StratoClim campaign database is available at https://halo-db.pa.op.dlr.de/mission/101. The BATAL balloon data is available at https://doi.org/10.15786/c.6379371.v1. The main modeling and figure data are available with a permanent DOI at Zhu (2024). The Community Earth System Model is available on the CESM trunk to any registered user: https://www.cesm.ucar.edu/models/cesm2/download (NCAR, 2023).

Acknowledgments
We thank J.P. Vernier, Jianghanyang Li, Chuck Brock, Doug Kinnison, Susan Solomon, Simon Clegg, Anthony Wexler for their valuable input. This research has been supported by the National Oceanic and Atmospheric Administration (Grant 03-01-07-001, NA17OAR4320101, and NA22OAR4320151). YZ and OBT acknowledge support from NSF Award No. AGS 1853932. NCAR's Community Earth System Model project is supported primarily by the National Science Foundation (NSF). This material is based upon work supported by the National Center for Atmospheric Research, which is a major facility sponsored by the NSF under Cooperative Agreement No. 1852977. Computing and data storage resources, including the Cheyenne supercomputer (https://doi.org/10.5065/D6RX99HX), were provided by the Computational and Information Systems Laboratory (CISL) at NCAR. The 2020 STeP SWOP campaign is supported by the Second Tibetan Plateau Scientific Expedition and Research Program (2019QZKK0604). The BATAL balloon-borne measurements were supported by the US National Aeronautics and Space Administration.

References

Appel, O., Köllner, F., Dragoneas, A., Hünig, A., Molleker, S., Schlager, H., et al. (2022). Chemical analysis of the Asian tropopause aerosol layer (ATAL) with emphasis on secondary aerosol particles using aircraft-based in situ aerosol mass spectrometry. *Atmospheric Chemistry and Physics*, *22*(20), 13607–13630. https://doi.org/10.5194/acp-22-13607-2022

Ayers, G. P., Gillett, R. W., & Gras, J. L. (1980). On the vapor pressure of sulfuric acid. *Geophysical Research Letters*, *7*(6), 433–436. https://doi.org/10.1029/GL007i006p00433

Bardeen, C. G., Toon, O. B., Jensen, E. J., Marsh, D. R., & Harvey, V. L. (2008). Numerical simulations of the three-dimensional distribution of meteoric dust in the mesosphere and upper stratosphere. *Journal of Geophysical Research*, *113*(D17), D17202. https://doi.org/10.1029/2007JD009515

Bela, M. M., Barth, M. C., Toon, O. B., Fried, A., Homeyer, C. R., Morrison, H., et al. (2016). Wet scavenging of soluble gases in DC3 deep convective storms using WRF-Chem simulations and aircraft observations. *Journal of Geophysical Research: Atmospheres*, *121*(8), 4233–4257. https://doi.org/10.1002/2015JD024623

Bian, J., Pan, L. L., Paulik, L., Vömel, H., Chen, H., & Lu, D. (2012). In situ water vapor and ozone measurements in Lhasa and Kunming during the Asian summer monsoon. *Geophysical Research Letters*, *39*(19), L19808. https://doi.org/10.1029/2012GL052996

Bossolasco, A., Jegou, F., Sellitto, P., Berthet, G., Kloss, C., & Legras, B. (2021). Global modeling studies of composition and decadal trends of the Asian Tropopause Aerosol Layer. *Atmospheric Chemistry and Physics*, *21*(4), 2745–2764. https://doi.org/10.5194/acp-21-2745-2021

Carslaw, K. S., Clegg, S. L., & Brimblecombe, P. (1995). A thermodynamic model of the system HCl-HNO_3-H_2SO_4-H_2O, including solubilities of HBr, from <200 to 328 K. *Journal of Physical Chemistry*, *99*(29), 11557–11574. https://doi.org/10.1021/j100029a039

Clegg, S. L., Brimblecombe, P., & Wexler, A. S. (1998). Thermodynamic model of the system $H^+-NH_4^+-SO_4^{2-}-NO_3^--H_2O$ at tropospheric temperatures. *The Journal of Physical Chemistry A*, *102*(12), 2137–2154. https://doi.org/10.1021/jp973042r

Clegg, S. L., Pitzer, K. S., & Brimblecombe, P. (1992). Thermodynamics of multicomponent, miscible, ionic solutions. Mixtures including unsymmetrical electrolytes. *Journal of Physical Chemistry*, *96*(23), 9470–9479. https://doi.org/10.1021/j100202a074

Costa, A., Meyer, J., Afchine, A., Luebke, A., Günther, G., Dorsey, J. R., et al. (2017). Classification of Arctic, midlatitude and tropical clouds in the mixed-phase temperature regime. *Atmospheric Chemistry and Physics*, *17*(19), 12219–12238. https://doi.org/10.5194/acp-17-12219-2017

Deshler, T. (2008). A review of global stratospheric aerosol: Measurements, importance, life cycle, and local stratospheric aerosol. *Atmospheric Research*, *90*(2–4), 223–232. https://doi.org/10.1016/j.atmosres.2008.03.016

Deshler, T. (2023). *University of Wyoming stratospheric aerosol measurements*. University of Wyoming. https://doi.org/10.15786/c.6379371.v1

Deshler, T., Hervig, M. E., Hofmann, D. J., Rosen, J. M., & Liley, J. B. (2003). Thirty years of in situ stratospheric aerosol size distribution measurements from Laramie, Wyoming (41°N), using balloon-borne instruments. *Journal of Geophysical Research*, *108*(D5), 4167. https://doi.org/10.1029/2002JD002514

Dragoneas, A., Molleker, S., Appel, O., Hünig, A., Böttger, T., Hermann, M., et al. (2022). The realization of autonomous, aircraft-based, real-time aerosol mass spectrometry in the upper troposphere and lower stratosphere. *Atmospheric Measurement Techniques*, *15*(19), 5719–5742. https://doi.org/10.5194/amt-15-5719-2022

Ebert, M., Weigel, R., Weinbruch, S., Schneider, L., Kandler, K., Lauterbach, S., et al. (2023). Characterization of refractory aerosol particles collected in the tropical UTLS within the Asian Tropopause Aerosol Layer (ATAL). *EGUsphere*, 1–45. https://doi.org/10.5194/egusphere-2023-2245

Fadnavis, S., Semeniuk, K., Pozzoli, L., Schultz, M. G., Ghude, S. D., Das, S., & Kakatkar, R. (2013). Transport of aerosols into the UTLS and their impact on the Asian monsoon region as seen in a global model simulation. *Atmospheric Chemistry and Physics*, *13*(17), 8771–8786. https://doi.org/10.5194/acp-13-8771-2013

Fischer, H., Birk, M., Blom, C., Carli, B., Carlotti, M., von Clarmann, T., et al. (2008). MIPAS: An instrument for atmospheric and climate research. *Atmospheric Chemistry and Physics*, *8*, 2151–2188. https://doi.org/10.5194/acp-8-2151-2008

Gao, R. S., Telg, H., McLaughlin, R. J., Ciciora, S. J., Watts, L. A., Richardson, M. S., et al. (2016). A light-weight, high-sensitivity particle spectrometer for PM2.5 aerosol measurements. *Aerosol Science and Technology*, *50*(1), 88–99. https://doi.org/10.1080/02786826.2015.1131809

Gu, Y., Liao, H., & Bian, J. (2016). Summertime nitrate aerosol in the upper troposphere and lower stratosphere over the Tibetan Plateau and the South Asian summer monsoon region. *Atmospheric Chemistry and Physics*, *16*(11), 6641–6663. https://doi.org/10.5194/acp-16-6641-2016

Hervig, M., & McHugh, M. (2002). Tropical nitric acid clouds. *Geophysical Research Letters*, *29*(7), 29-21–29-24. https://doi.org/10.1029/2001GL014271

Holloway, C. E., & Neelin, J. D. (2007). The convective cold top and quasi equilibrium. *Journal of the Atmospheric Sciences*, *64*(5), 1467–1487. https://doi.org/10.1175/JAS3907.1

Höpfner, M., Ungermann, J., Borrmann, S., Wagner, R., Spang, R., Riese, M., et al. (2019). Ammonium nitrate particles formed in upper troposphere from ground ammonia sources during Asian monsoons. *Nature Geoscience*, *12*(8), 608–612. https://doi.org/10.1038/s41561-019-0385-8

Höpfner, M., Volkamer, R., Grabowski, U., Grutter, M., Orphal, J., Stiller, G., et al. (2016). First detection of ammonia (NH_3) in the Asian summer monsoon upper troposphere. *Atmospheric Chemistry and Physics*, *16*(22), 14357–14369. https://doi.org/10.5194/acp-16-14357-2016

Hünig, A., Appel, O., Dragoneas, A., Molleker, S., Clemen, H. C., Helleis, F., et al. (2022). Design, characterization, and first field deployment of a novel aircraft-based aerosol mass spectrometer combining the laser ablation and flash vaporization techniques. *Atmospheric Measurement Techniques*, *15*(9), 2889–2921. https://doi.org/10.5194/amt-15-2889-2022

Jost, A., Szakáll, M., Diehl, K., Mitra, S. K., & Borrmann, S. (2017). Chemistry of riming: The retention of organic and inorganic atmospheric trace constituents. *Atmospheric Chemistry and Physics*, *17*(16), 9717–9732. https://doi.org/10.5194/acp-17-9717-2017

Kim, J., Randel, W. J., & Birner, T. (2018). Convectively driven tropopause-level cooling and its influences on stratospheric moisture. *Journal of Geophysical Research: Atmospheres*, *123*(1), 590–606. https://doi.org/10.1002/2017JD027080

Krämer, M., Rolf, C., Luebke, A., Afchine, A., Spelten, N., Costa, A., et al. (2016). A microphysics guide to cirrus clouds—Part 1: Cirrus types. *Atmospheric Chemistry and Physics*, *16*(5), 3463–3483. https://doi.org/10.5194/acp-16-3463-2016

Krämer, M., Rolf, C., Spelten, N., Afchine, A., Fahey, D., Jensen, E., et al. (2020). A microphysics guide to cirrus—Part 2: Climatologies of clouds and humidity from observations. *Atmospheric Chemistry and Physics*, *20*(21), 12569–12608. https://doi.org/10.5194/acp-20-12569-2020

Li, D., Vogel, B., Bian, J., Müller, R., Pan, L. L., Günther, G., et al. (2017). Impact of typhoons on the composition of the upper troposphere within the Asian summer monsoon anticyclone: The SWOP campaign in Lhasa 2013. *Atmospheric Chemistry and Physics*, *17*(7), 4657–4672. https://doi.org/10.5194/acp-17-4657-2017

Lin, J.-S., & Tabazadeh, A. (2001). A parameterization of an aerosol physical chemistry model for the $NH_3/H_2SO_4/HNO_3/H_2O$ system at cold temperatures. *Journal of Geophysical Research*, *106*(D5), 4815–4829. https://doi.org/10.1029/2000JD900598

Lin, J.-S., & Tabazadeh, A. (2002). The effect of nitric acid uptake on the deliquescence and efflorescence of binary ammoniated salts in the upper troposphere. *Geophysical Research Letters*, *29*(10), 126-121–126-124. https://doi.org/10.1029/2002GL015251

Luo, B., Carslaw, K. S., Peter, T., & Clegg, S. L. (1995). Vapour pressures of $H_2SO_4/HNO_3/HCl/HBr/H_2O$ solutions to low stratospheric temperatures. *Geophysical Research Letters*, *22*(3), 247–250. https://doi.org/10.1029/94GL02988

Mahnke, C., Weigel, R., Cairo, F., Vernier, J. P., Afchine, A., Krämer, M., et al. (2021). The Asian tropopause aerosol layer within the 2017 monsoon anticyclone: Microphysical properties derived from aircraft-borne in situ measurements. *Atmospheric Chemistry and Physics*, *21*(19), 15259–15282. https://doi.org/10.5194/acp-21-15259-2021

Massucci, M., Clegg, S. L., & Brimblecombe, P. (1999). Equilibrium partial pressures, thermodynamic properties of aqueous and solid phases, and Cl_2 production from aqueous HCl and HNO_3 and their mixtures. *The Journal of Physical Chemistry A*, *103*(21), 4209–4226. https://doi.org/10.1021/jp9847179

Mills, M. J., Schmidt, A., Easter, R., Solomon, S., Kinnison, D. E., Ghan, S. J., et al. (2016). Global volcanic aerosol properties derived from emissions, 1990–2014, using CESM1(WACCM). *Journal of Geophysical Research: Atmospheres*, *121*(5), 2332–2348. https://doi.org/10.1002/2015JD024290

NCAR CESM model. (2023). Retrieved from https://www.cesm.ucar.edu/models/cesm2/download

Neely, I. I. I., Ryan, R., & Schmidt, A. (2016). VolcanEESM: Global volcanic sulphur dioxide (SO_2) emissions database from 1850 to present [Dataset]. *Centre for Environmental Data Analysis*. https://doi.org/10.5285/76ebdc0b-0eed-4f70-b89e-55e606bcd568

Neely, R. R., III., Toon, O. B., Solomon, S., Vernier, J.-P., Alvarez, C., English, J. M., et al. (2013). Recent anthropogenic increases in SO_2 from Asia have minimal impact on stratospheric aerosol. *Geophysical Research Letters*, *40*(5), 999–1004. https://doi.org/10.1002/grl.50263

Pan, L. L., Atlas, E. L., Honomichl, S. B., Smith, W. P., Kinnison, D. E., Solomon, S., et al. (2024). East Asian summer monsoon delivers large abundances of very short-lived organic chlorine substances to the lower stratosphere. *Proceedings of the National Academy of Sciences of the United States of America*, *121*(12), e2318716121. https://doi.org/10.1073/pnas.2318716121

Pan, L. L., Honomichl, S. B., Kinnison, D. E., Abalos, M., Randel, W. J., Bergman, J. W., & Bian, J. (2016). Transport of chemical tracers from the boundary layer to stratosphere associated with the dynamics of the Asian summer monsoon. *Journal of Geophysical Research: Atmospheres*, *121*(23), 14159–14174. https://doi.org/10.1002/2016JD025616

Pan, L. L., Kinnison, D., Liang, Q., Chin, M., Santee, M. L., Flemming, J., et al. (2022). A multimodel investigation of Asian summer monsoon UTLS transport over the western Pacific. *Journal of Geophysical Research: Atmospheres*, *127*(24), e2022JD037511. https://doi.org/10.1029/2022JD037511

Park, M., Randel, W. J., Emmons, L. K., & Livesey, N. J. (2009). Transport pathways of carbon monoxide in the Asian summer monsoon diagnosed from Model of Ozone and Related Tracers (MOZART). *Journal of Geophysical Research*, *114*(D8), D08303. https://doi.org/10.1029/2008JD010621

Randel, W. J., & Park, M. (2006). Deep convective influence on the Asian summer monsoon anticyclone and associated tracer variability observed with Atmospheric Infrared Sounder (AIRS). *Journal of Geophysical Research*, *111*(D12), D12314. https://doi.org/10.1029/2005JD006490

Randel, W. J., Park, M., Emmons, L., Kinnison, D., Bernath, P., Walker, K. A., et al. (2010). Asian monsoon transport of pollution to the stratosphere. *Science*, *328*(5978), 611–613. https://doi.org/10.1126/science.1182274

Randel, W. J., Wu, F., & Rivera Ríos, W. (2003). Thermal variability of the tropical tropopause region derived from GPS/MET observations. *Journal of Geophysical Research*, *108*(D1), ACL7-1–ACL7-12. https://doi.org/10.1029/2002JD002595

Randel, W. J., Zhang, K., & Fu, R. (2015). What controls stratospheric water vapor in the NH summer monsoon regions? *Journal of Geophysical Research: Atmospheres*, *120*(15), 7988–8001. https://doi.org/10.1002/2015JD023622

Rienecker, M. M., Suarez, M. J., Todling, R., Bacmeister, J., Takacs, L., Liu, H. C., et al. (2008). *The GEOS-5 data assimilation system—Documentation of versions 5.0.1, 5.1.0, and 5.2.0* (No. NASA/TM-2008-104606-VOL-27).

Schill, G., Murphy, D., Lawler, M., & Abou-Ghanem, M. (2023). Single-particle aerosol composition in the Asian tropopause aerosol layer and in the North American upper troposphere/lower stratosphere during ACCLIP. In *EGU General Assembly* (p. EGU23-9792). https://doi.org/10.5194/egusphere-egu23-9792

Shi, Q., Jayne, J. T., Kolb, C. E., Worsnop, D. R., & Davidovits, P. (2001). Kinetic model for reaction of $ClONO_2$ with H_2O and HCl and HOCl with HCl in sulfuric acid solutions. *Journal of Geophysical Research*, *106*(D20), 24259–24274. https://doi.org/10.1029/2000JD000181

Solomon, S., Kinnison, D., Garcia, R. R., Bandoro, J., Mills, M., Wilka, C., et al. (2016). Monsoon circulations and tropical heterogeneous chlorine chemistry in the stratosphere. *Geophysical Research Letters*, *43*(12), 12624–12633. https://doi.org/10.1002/2016GL071778

Solomon, S., Stone, K., Yu, P., Murphy, D. M., Kinnison, D., Ravishankara, A. R., & Wang, P. (2023). Chlorine activation and enhanced ozone depletion induced by wildfire aerosol. *Nature*, *615*(7951), 259–264. https://doi.org/10.1038/s41586-022-05683-0

Thomason, L. W., & Vernier, J. P. (2013). Improved SAGE II cloud/aerosol categorization and observations of the Asian tropopause aerosol layer: 1989–2005. *Atmospheric Chemistry and Physics*, *13*(9), 4605–4616. https://doi.org/10.5194/acp-13-4605-2013

Tilmes, S., Mills, M. J., Zhu, Y., Bardeen, C. G., Vitt, F., Yu, P., et al. (2023). Description and performance of a sectional aerosol microphysical model in the Community Earth System Model (CESM2). *Geoscientific Model Development*, *16*(21), 6087–6125. https://doi.org/10.5194/gmd-16-6087-2023

Toon, O. B., Turco, R. P., Westphal, D., Malone, R., & Liu, M. (1988). A multidimensional model for aerosols: Description of computational analogs. *Journal of the Atmospheric Sciences*, *45*(15), 2123–2144. https://doi.org/10.1175/1520-0469(1988)045<2123:AMMFAD>2.0.CO;2

Vernier, H., Rastogi, N., Liu, H., Pandit, A. K., Bedka, K., Patel, A., et al. (2022). Exploring the inorganic composition of the Asian Tropopause Aerosol Layer using medium-duration balloon flights. *Atmospheric Chemistry and Physics*, *22*(18), 12675–12694. https://doi.org/10.5194/acp-22-12675-2022

Vernier, J.-P., Fairlie, T. D., Deshler, T., Venkat Ratnam, M., Gadhavi, H., Kumar, B. S., et al. (2018). BATAL: The balloon measurement campaigns of the Asian tropopause aerosol layer. *Bulletin of the American Meteorological Society*, *99*(5), 955–973. https://doi.org/10.1175/BAMS-D-17-0014.1

Vernier, J.-P., Thomason, L. W., & Kar, J. (2011). CALIPSO detection of an Asian tropopause aerosol layer. *Geophysical Research Letters*, *38*(7), L07804. https://doi.org/10.1029/2010GL046614

Wang, M., Xiao, M., Bertozzi, B., Marie, G., Rörup, B., Schulze, B., et al. (2022). Synergistic $HNO_3–H_2SO_4–NH_3$ upper tropospheric particle formation. *Nature*, *605*(7910), 483–489. https://doi.org/10.1038/s41586-022-04605-4

Wang, P.-H., Minnis, P., McCormick, M. P., Kent, G. S., & Skeens, K. M. (1996). A 6-year climatology of cloud occurrence frequency from Stratospheric Aerosol and Gas Experiment II observations (1985–1990). *Journal of Geophysical Research*, *101*(D23), 29407–29429. https://doi.org/10.1029/96JD01780

Weigel, R., Hermann, M., Curtius, J., Voigt, C., Walter, S., Böttger, T., et al. (2009). Experimental characterization of the COndensation PArticle counting System for high altitude aircraft-borne application. *Atmospheric Measurement Techniques*, *2*(1), 243–258. https://doi.org/10.5194/amt-2-243-2009

Weigel, R., Mahnke, C., Baumgartner, M., Dragoneas, A., Vogel, B., Ploeger, F., et al. (2021). In situ observation of new particle formation (NPF) in the tropical tropopause layer of the 2017 Asian monsoon anticyclone—Part 1: Summary of StratoClim results. *Atmospheric Chemistry and Physics*, *21*(15), 11689–11722. https://doi.org/10.5194/acp-21-11689-2021

Weigel, R., Mahnke, C., Baumgartner, M., Krämer, M., Spichtinger, P., Spelten, N., et al. (2021). In situ observation of new particle formation (NPF) in the tropical tropopause layer of the 2017 Asian monsoon anticyclone—Part 2: NPF inside ice clouds. *Atmospheric Chemistry and Physics*, *21*(17), 13455–13481. https://doi.org/10.5194/acp-21-13455-2021

Wexler, A. S., & Clegg, S. L. (2002). Atmospheric aerosol models for systems including the ions H^+, ${NH_4}^+$, Na^+, ${SO_4}^{2-}$, ${NO_3}^-$, Cl^-, Br^-, and H_2O. *Journal of Geophysical Research*, *107*(D14), ACH14-11–ACH14-14. https://doi.org/10.1029/2001JD000451

Yang, K., Wang, Z., Luo, T., Liu, X., & Wu, M. (2022). Upper troposphere dust belt formation processes vary seasonally and spatially in the Northern Hemisphere. *Communications Earth & Environment*, *3*(1), 24. https://doi.org/10.1038/s43247-022-00353-5

Yu, P., Lian, S., Zhu, Y., Toon, O. B., Höpfner, M., & Borrmann, S. (2022). Abundant nitrate and nitric acid aerosol in the upper troposphere and lower stratosphere. *Geophysical Research Letters*, *49*(18), e2022GL100258. https://doi.org/10.1029/2022GL100258

Yu, P., Rosenlof, K. H., Liu, S., Telg, H., Thornberry, T. D., Rollins, A. W., et al. (2017). Efficient transport of tropospheric aerosol into the stratosphere via the Asian summer monsoon anticyclone. *Proceedings of the National Academy of Sciences of the United States of America*, *114*(27), 6972–6977. https://doi.org/10.1073/pnas.1701170114

Yu, P., Toon, O. B., Bardeen, C. G., Mills, M. J., Fan, T., English, J. M., & Neely, R. R. (2015). Evaluations of tropospheric aerosol properties simulated by the community Earth system model with a sectional aerosol microphysics scheme. *Journal of Advances in Modeling Earth Systems*, *7*(2), 865–914. https://doi.org/10.1002/2014MS000421

Zaveri, R. A., Easter, R. C., Fast, J. D., & Peters, L. K. (2008). Model for simulating aerosol interactions and chemistry (MOSAIC). *Journal of Geophysical Research*, *113*(D13), D13204. https://doi.org/10.1029/2007JD008782

Zhu, Y. (2024). ATAL [Dataset]. https://doi.org/10.17605/OSF.IO/Y96MW

Zhu, Y., Toon, O. B., Lambert, A., Kinnison, D. E., Brakebusch, M., Bardeen, C. G., et al. (2015). Development of a polar stratospheric cloud model within the community Earth system model using constraints on type I PSCs from the 2010–2011 Arctic winter. *Journal of Advances in Modeling Earth Systems*, *7*(2), 551–585. https://doi.org/10.1002/2015MS000427